Elucidating the origins of path hysteresis during electrochemical cycling of Li-Sb electrodes

Donghee Chang,[†,‡] Hua Huo,[¶] Karen E. Johnston,[¶] Cyril Marino,[§] Laure Monconduit,[§] Clare P. Grey,[¶] and Anton Van der Ven[*,‡]

Department of Materials Science and Engineering, University of Michigan, Ann Arbor, Michigan, 48109, USA, Materials Department, University of California Santa Barbara, 1361A, Engineering II, Santa Barbara, CA, 93106-5050, USA, 3Department of Chemistry, University of Cambridge, Lensfield Road, Cambridge, CB2 1EW, UK, and Institut Charles Gerhardt Montpellier-UMR 5253 CNRS, ALISTORE European Research Institute (3104 CNRS), Universitï£¡ Montpellier 2, 34095, Montpellier, France

E-mail: avdv@engineering.ucsb.edu

Abstract

We investigate the origins of phase transformation hysteresis in electrodes of Li-ion batteries, focusing on the alloying reaction of Li with Sb. Electrochemical measurements confirm that the reaction path followed during Li insertion into Sb electrodes differs from that followed upon subsequent Li extraction. We use a combination of first-principles calculations and NMR studies to establish the electronic, thermodynamic and kinetic properties of Sb, Li_2Sb and Li_3Sb, three phases that can coexist as Li reacts with Sb. Results from first-principles calculations along with NMR measurements indicate that both Li_2Sb and Li_3Sb are capable of tolerating high Li-vacancy conentrations. We identify a lever effect in the driving force for nucleation that favors the nucleation of phases with large changes in Li concentration over phases that are globally stable. This lever effect is especially pronounced in the Li-Sb system, which, together with a very high Li mobility in Li_3Sb that can facilitate high over potentials, provides an explanation for the observed path hysteresis between charge and discharge.

1 Introduction

Most electrochemically active electrode materials used in Li and Na batteries are intercalation compounds that are capable of accommodating large variations in Li and Na ion concentration.[1,2] Electrochemically viable intercalation compounds, many of them relying on a valence shift of a transition metal ion, maintain the same host crystal structure and undergo only minor variations in lattice parameters as either the Li or Na concentration is varied. Electrochemical cycling can therefore occur without substantial degradation. Although ideal in many ways for electrochemical energy storage applications, intercalation compounds nevertheless have a limited capacity as measured by the amount of Li or Na that can be removed and reinserted into the compound.

Alternative solid-state reaction mechanisms that differ qualitatively from intercalation processes are also possible. An important class includes displacement and conversion reactions whereby the extrusion and subsequent precipitation of a transition metal cation occurs simultaneously with the insertion of Li (or Na).[3–5] This mechanism allows for the exploitation of a multi-electron valence shift to achieve very high capacities. Even higher theoretical capacities are possible if the transition metal is eliminated altogether. The Li (or Na) then reacts directly with another element. Li-air and Li-sulfur[6–9] batteries fall in this category, as do electrodes that rely on alloying reactions with

Si, Sn, Al and Sb among others.[10–12] The reaction of Li with Si and Sn, for example, can yield compounds with very high Li concentrations (i.e. $Li_{4.4}Si$ and $Li_{4.4}Sn$) making capacities as high as 4200 $mAhg^{-1}$and 993 $mAhg^{-1}$theoretically possible.[10,13,14]

While enabling higher capacities, reaction mechanisms that go beyond intercalation often exhibit a large hysteresis in the voltage profile between charge and discharge. A sizable hysteresis leads to unacceptable energy losses during cycling. It is a major impediment to the commercialization of otherwise promising high-capacity electrode chemistries. A fundamental understanding of the factors that cause hysteresis in electrodes undergoing complex solid-state reaction mechanisms is still quite limited.

There are several sources of hysteresis in solid-state electrochemical reactions. One is purely dissipative and emerges from sluggish kinetics on the time scale of the charge and discharge cycle. Slowing the charge and discharge rate can systematically reduce this form of polarization. Hysteresis in the voltage profile will also emerge if the reaction follows a different path during discharge compared to that followed during charge.[15,16] The resulting path hysteresis arises due to an asymmetry in competing kinetic mechanisms and becomes more likely as the number of accessible kinetic mechanisms of ion insertion/removal increases.[16] A third source of hysteresis can arise due to mechanical dissipation, either when coherency strains need to be overcome during two-phase coexistence[17] or in the form of plastic deformation, likely an important factor in some alloying reactions undergoing large volume changes.[18]

The aim of this study is to shed light on the causes of hysteresis in electrodes of Li-ion batteries undergoing alloying reactions with a particular focus on Sb electrodes. Sb has a specific capacity of 660 $mAhg^{-1}$and undergoes smaller volume changes and fewer phase transformations than Si and Sn when reacting with Li. The electrochemical reaction of Li with Sb electrodes is also accompanied by path hysteresis with the discharge voltage profile qualitatively differing in shape from the charge profile. Lithium insertion into Sb electrodes leads first to the formation of Li_2Sb having hexagonal symmetry followed by the formation of Li_3Sb having cubic symmetry.[19,20] Upon Li removal, however, Li_3Sb transforms directly to Sb, bypassing the intermediate hexagonal Li_2Sb phase.[19,20] Hence the discharge voltage curve has two plateaus separated by a small step at the Li_2Sb composition, while the charge profile has one plateau, which is usually about 0.2-0.3 V above the discharge plateaus. The hysteresis persists even at low charge and discharge rates. In spite of this path hysteresis, the charge and discharge profiles as well as the capacity does not change much over many cycles,[21] in contrast to bulk Si and Sn electrodes, which can show large irreversible capacity losses.[10,14]

With the aim of elucidating the origin of the path hysteresis exhibited by the alloying reaction of Li with Sb, we combine first-principles calculations with electrochemical and NMR studies to establish a range of crystallographic, electronic, thermodynamic and kinetic properties of the three phases that form during the electrochemical reaction of Li with Sb. Based on these property predictions we argue that path hysteresis in Sb electrodes arises from an asymmetry in the competition between Li diffusion rates and driving forces for nucleation.

2 Experimental and Computational Methods

Computational Methods

First-principles electronic structure calculations were performed using density functional theory (DFT) within the generalized gradient approximation as parameterized by Perdew-Burke-Ernzerhof (PBE).[22] We used the Vienna Ab initio simulation package (VASP) plane wave pseudopotential code[23,24] with the projector augmented wave method (PAW) to describe the interactions between valence and core electrons.[25,26] An energy cutoff of 400 eV was used. We used a Γ-point centered $12\times12\times12$ k-point mesh for the primitive cell of Li_3Sb, a $6\times6\times6$ k-point mesh for the unit cell of Li_2Sb and a $12\times12\times4$ mesh for the unit cell of Sb. The k-point meshes for supercells of these structures were chosen to yield a similar k-point density in reciprocal space. Ionic positions and the lattice parameters of each structure were

fully relaxed.

To study off stoichiometry at room temperature (as opposed to 0 K), we also performed a statistical mechanical study of the thermodynamic properties using cluster expansion Hamiltonians and Monte Carlo simulations. We used the CASM software package[27,28] to construct the cluster expansions and parameterize their coefficients to first-principles total energy calculations as well as to perform Monte Carlo simulations.

Lithium migration mechanisms and barriers were determined using the climbing image nudged-elastic-band method[29] as implemented in VASP. For each phase, a large supercell was used, allowing all atoms to relax while holding the lattice parameters and volume of the supercell fixed.

To calculate electronic densities of state and band structure of A7 Sb, hexagonal Li_2Sb and cubic Li_3Sb we used the HSE06 hybrid functional.[30]

Electrode Preparation

All electrodes for ex situ ^{7}Li NMR studies were prepared as self-supporting films using carboxymethyl cellulose (CMC) (degree of substitution DS = 0.7, and average molecular weight M_w = 250,000 g mol^{-1}, Aldrich) as a binder with two conductive additives: (i) vapor-grown carbon fibers (VGCF, diameter 100-200 nm and length 10-20 μm, Brunauer-Emmett-Teller (BET) surface areas 15 m^{2}g^{-1}, SHOWA DENKO) and (ii) carbon black Y50A (CB, BET primary particle size 20-60 nm, primary aggregate size 100 nm, surface area 70 m^{2}g^{-1}).The Sb powder (350 mesh, 99.5%, Alfa Aesar), CMC, and additives were manually ground in a mortar and pestle with a weight ratio of 10/12/9/9% (Sb/CMC/Y50A/VGCF). The mixture was then mixed with deionised water in a silicon nitride vial containing three 9.5 mm diameter silicon nitride balls. A Fritsch Pulverisette 7 was used to mill the mixture at 500 rpm for 1 hour. The slurry was tape cast onto 22 μm thick copper foil at 150 μm thickness. The electrodes were then dried for 12 hours at room temperature and 1 hour at 100 °C under vacuum. To prepare electrodes for *in situ* NMR, the slurry was cast onto one end of a pre-weighed strip of copper mesh, leaving the uncoated side to serve as the battery lead.

Electrochemical Tests

All *ex situ* NMR measurements were completed in 2032-type coin cells. Sb electrodes were cycled against Li metal with 1 M $LiPF_6$ dissolved in a 1:1 volumetric mixture of ethylene carbonate (EC) and dimethyl carbonate (DMC). Each cell was assembled inside an argon-filled glovebox. Electrochemical curves were recorded on an Arbin Instrument at room temperature under galvanostatic conditions. After electrochemical cycling, the cells were disassembled in a glovebox, where the active materials were extracted and packed into zirconia rotors for NMR analysis.

For all *in situ* NMR studies a flexible battery design was used, where the positive electrode was prepared using the method described above.[31] The negative electrode was constructed by pressing lithium metal onto copper mesh, leaving bare copper mesh at one end to act as the battery lead. A VSP cycler (Bio-Logic) was used for cycling the *in situ* cells.

Solid-State NMR Spectroscopy

***Ex situ* NMR Data** All room temperature ^{6,7}Li static and magic-angle spinning (MAS) NMR spectra were acquired using a Bruker Avance 400 MHz spectrometer, equipped with a wide-bore 9.4 T magnet using Larmor frequencies of 58.88 MHz and 155.51 MHz for ^{6}Li (I = 1) and ^{7}Li (I = 3/2), respectively. The powdered samples were packed into conventional 2.5 mm zirconia rotors and a MAS rate of 30 kHz was employed. A rotor-synchronized Echo-MAS sequence was used (90°-τ-180°-τ). Two-dimensional magnetization exchange ^{6,7}Li NMR spectra were acquired using the sequence (π/2)-τ_1-(π/2)-τ_m-(π/2)-τ_2-acq, where τ_1 and τ_2 represent interpulse delays and ?m is the mixing time. A range of mixing times were tested, including 0.1, 10, 50 and 200 ms.

***In situ* NMR Data** All static ^{7}Li NMR spectra were acquired using a Tecmag 300 MHz spectrometer, equipped with a wide-bore 7 T magnet using a Larmor frequency of 116.64 MHz. Single pulse experiments with a recycle delay of 1 s were employed using a static probe equipped with a 1 cm coil. To improve the signal-to-noise ratio of the ^{7}Li NMR spectra, low-pass filters (50 MHz)

were used to filter any high-frequency noise arising from the cycler. All ^{6,7}Li chemical shifts were referenced to 1 M LiCl (aq) at δ_{iso} = 0 ppm.

3 Results

3.1 Crystallography

There are three distinct phases that can coexist when Li alloys with Sb. The first is pure Sb, prototype A7, which belongs to space group R$\bar{3}$m (No.166).[32] Its crystal structure is shown in Figure 1a and consists of puckered layers. The second phase is hexagonal Li_2Sb belonging to space group P$\bar{6}$2c (No.190)[33] and is shown in Figure 1b. The last phase is Li_3Sb which has cubic symmetry and belongs to space group Fm$\bar{3}$m (No.225).[32,34]

Sb, Li_2Sb and Li_3Sb can each be described as the stacking of either triangular Sb layers or a combination of triangular and honeycomb Sb layers. Following convention, we denote stacking sequences of triangular layers with the letters A, B and C. To emphasize that these layers are triangular lattices, we add a subscript t such that the stacking in fcc, for example, would be denoted by $A_tB_tC_t$. There are also several ways of stacking a honeycomb network, which can also be denoted by the letters A, B and C. For a honeycomb layer, we add the subscript h. In describing the crystallographic relationships between Sb, Li_2Sb and Li_3Sb, we will also need to distinguish between layers that have been rotated by 30 degrees around an axis perpendicular to the layer. We label these layers with a prime, e.g. A'$_t$.

The crystal structure of pure Sb is similar to the fcc lattice except that every other close-packed (111) layer is off-centered. Figure 1c illustrates the Sb crystal structures as represented by layers of triangular lattices. The triangular lattices have an $A_tB_tC_t$ stacking sequence as in fcc, but with non-uniform spacing between pairs of planes. The off-centering of alternating layers allows the Sb of one close-packed plane to form three short bonds with neighboring Sb of the other close-packed plane (Figure 1a).

The crystal structure of hexagonal Li_2Sb is also layered in the sense that the Sb sublattice can be described as consisting of two-dimensional honeycomb layers, A_h, interleaved by two-dimensional triangular lattices, A$_t$'. The Sb-Sb nearest neighbor distance within the A'$_t$ layers of Li_2Sb is substantially larger than that in the triangular layers of pure Sb as they reside above and below the centers of the honeycomb rings of the adjacent A_h layers. The Sb sublattice is identical to the omega phase of elemental metals such as Ti and Zr and their suboxides.[35,36] The Li ions occupy two symmetrically distinct interstitial sites within this Sb sublattice. The first is a five-fold coordinated square pyramidal site (6h Wyckoff position), while the second is a four fold coordinated tetrahedral site (6g Wyckoff position).

The Sb sublattice of Li_3Sb forms a perfect fcc lattice, which is a stacking of close-packed triangular lattices, i.e. $A_tB_tC_t$. The Li ions occupy all the octahedral and tetrahedral interstitial sites of the fcc Sb sublattice.

Although several crystallographic pathways linking A7 Sb to the Sb sublattice of the hexagonal Li_2Sb phase can be identified, one is especially straightforward. It relies on the splitting of each triangular lattice of Sb into a honeycomb layer and a new triangular lattice that is rotated by 30 degrees and has a much larger nearest neighbor distance between Sb. An A_t layer of pure Sb, for example, can split into a A_h honeycomb layer and a A'$_t$ layer as illustrated in Figure 1c. The Sb atoms of A_t that ultimately form the A'$_t$ triangular lattice form a $\sqrt{3} \times \sqrt{3}$ supercell in the original A_t layer. If every triangular layer splits in this manner, an intermediate crystal is formed with $A_hA'_tB_hB'_tC_hC'_t$ stacking as illustrated in Figure 1c. This intermediate crystal must be sheared to obtain the $A_hA'_tA_hA'_tA_hA'_t$ of the Sb sub lattice in Li_2Sb as shown in Figure 1c.

A similar mechanism connects the Sb sublattice of Li_2Sb with that of Li_3Sb. The collapse of a honeycomb network A_h with a triangular lattice A'$_t$ forms a triangular lattice A_t. The collapse of pairs of A_h and A'$_t$ must also be accompanied by a shear to take the resulting $A_tA_tA_t$ stacking to an fcc $A_tB_tC_t$ stacking characterizing the Sb sublattice of Li_3Sb.

In view of the crystallographic similarities between the three phases the possibility exists that the two-phase reactions between any pair of them could occur coherently. An important metric to an-

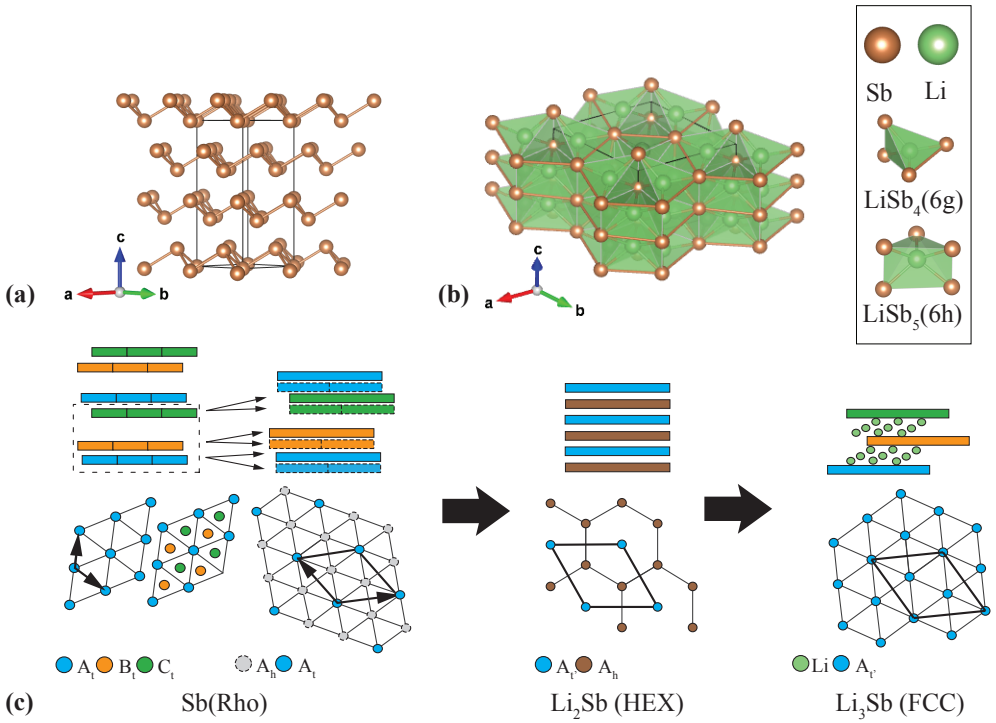

Figure 1: Crystal structures of (a) pure A7 Sb ($R\bar{3}m$) and (b) hexagonal Li_2Sb ($P\bar{6}2c$). (c) Schematic illustrations of structural transformations from Sb to Li_2Sb and from Li_2Sb to Li_3Sb. A_t,B_t, and C_t represent triangular lattices and A_h represents a honeycomb network. A'$_t$ represents a triangular lattice rotated by 30 degrees.

alyze this possibility is the transformation strain required to deform one crystal into the other. If the transformation strain is small the two-phase reaction may proceed coherently without incurring large coherency strain energy penalties. The transformation strain can be defined using the starting phase as the reference. The Green-Lagrange strain tensor, E, is related to the deformation gradient $\hat{F}$ according to

$$E = \frac{\hat{F}^{+}\hat{F} - I}{2} \qquad (1)$$

where, for homogeneous strain, the 3x3 deformation gradient matrix $\hat{F}$ relates the lattice vectors of the transformed crystal $\mathbf{a}'$, $\mathbf{b}'$ and $\mathbf{c}'$ to the lattice vectors of the original crystal $\mathbf{a}$, $\mathbf{b}$ and $\mathbf{c}$ according to $\mathbf{a}' = \hat{F}\mathbf{a}$. $\hat{F}^{+}$ corresponds to the transpose of $\hat{F}$.

In general, large misfit strains between the original crystal structure and the new crystal structure will incur large strain energy costs when the two phases coexist coherently. If this strain energy is larger than the cost of forming an incoherent interface, the transformation will occur reconstructively. As is to be expected for alloying reactions, the volume changes in the Li-Sb system are very large. Transforming from Sb to Li_2Sb results in a volume change of close to 90%, while the addition of Li to Li_2Sb to form Li_3Sb results in a further increase of about 35% relative to the Sb volume. Large volume changes by themselves, though, do not necessarily result in strain energy penalties. There are special anisotropic transformation strains in which particular crystallographic planes do not undergo a strain as the original crystal transforms into the new crystal. The transformation can then proceed coherently in the absence of coherency strains if the interface separating the growing phase from the original phase within an electrode particle is parallel to these strain invariant planes. The requirement for the existence of a strain invariant plane is that one eigenvalue of E is equal to 0, one eigenvalue is greater than 0 and one eigenvalue is less than 0.[37]

The eigenvalues of the transformation strains, Eq. 1, assuming the crystallographic transformation paths described above and using experimentally measured lattice parameters[32,33] are listed in Table 1. The transformation strains are very large as is clear by the large eigenvalues. However,

they all show at least one positive and one negative eigenvalue as well as an eigenvalue close to zero. Nevertheless, the eigenvalues close to zero are still sizable and thus none of the transformation strains exhibit a strict strain invariant plane. If any of these transformations occur coherently, they will be accompanied by coherency strain. We point out though that the transformations that most closely approach the conditions for a strain invariant plane are between Li_2Sb and Li_3Sb.

Table 1: The eigenvalues of the transformation strains for various crystallographic transformation paths using experimentally measured lattice parameters

Transformation path	λ_1	λ_2	λ_3
$Sb \rightarrow Li_2Sb$	-0.0416	0.0669	1.3652
$Sb \rightarrow Li_3Sb$	-0.1031	0.0817	2.4883
$Li_2Sb \rightarrow Li_3Sb$	-0.2224	0.0130	0.7493
$Li_2Sb \rightarrow Sb$	-0.3660	-0.0590	0.0453
$Li_3Sb \rightarrow Li_2Sb$	-0.2999	-0.0127	0.4007
$Li_3Sb \rightarrow Sb$	-0.4163	-0.0702	0.1299

3.2 First-Principles Results

Electronic structure

The electrodes of an electrochemical cell should exhibit some degree of electronic conductivity such that electrons can reach the electrode/electrolyte interface where the electrochemical reactions occur. We used both DFT-PBE as well as HSE06[30] to calculate the electronic densities of state and band structure of A7 Sb, hexagonal Li_2Sb and cubic Li_3Sb. The densities of states and band structure as calculated with HSE06 are shown in Figure 2. Both A7 Sb and cubic Li_3Sb are predicted to be semi-conductors having band gaps of approximately 0.05 and 1.1 eV respectively. Hexagonal Li_2Sb is predicted to be metallic with the Fermi level close to a minimum in the density of states.

Lithium removal from cubic Li_3Sb lowers the Fermi level into the valence band resulting in the creation of holes. The density of states rises sharply when decreasing the Fermi level away from the valence band maximum. This suggests that the holes, created upon Li removal, will likely

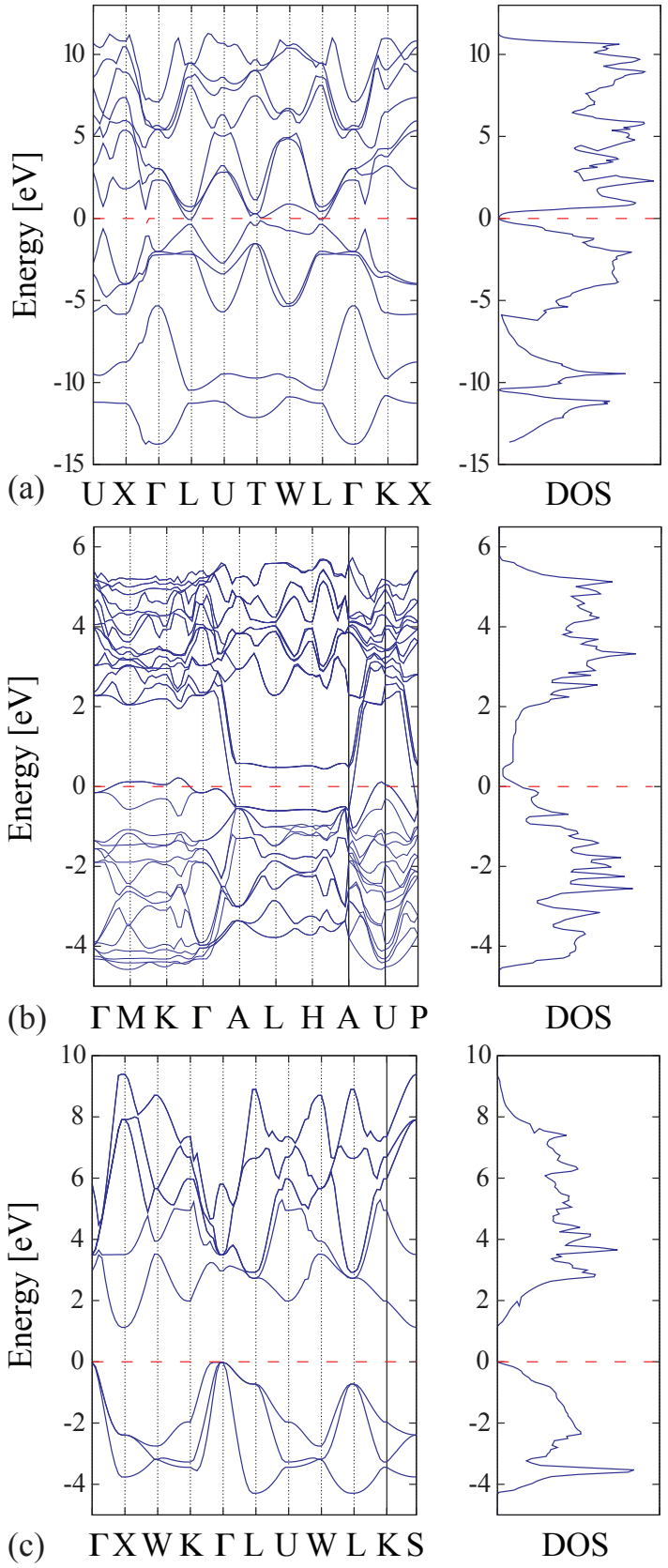

Figure 2: Calculated electronic densities of state and band structures of (a) A7 Sb (rhombohedral unit cell), (b) Li_2Sb, and (c) Li_3Sb using the HSE screened hybrid functional. The Fermi level is set to zero.

form itinerant states that are mobile, very quickly making $Li_{3-y}Sb$ electronically conducting.

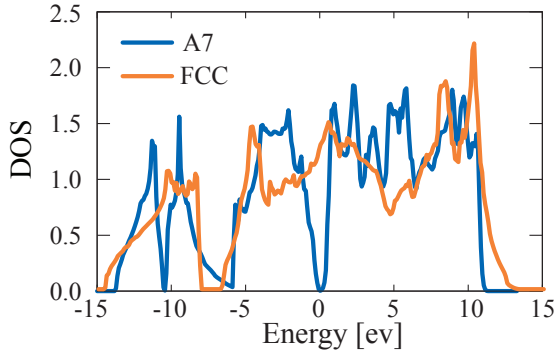

Figure 3: Density of states of the A7 form of Sb (blue) and the perfect fcc form of Sb (orange). The A7 form of Sb is similar to the fcc lattice with the exception that every other close-packed(111) layer is off-centered.

The band gap of A7 Sb is predicted to be very small. As described above, the A7 form of Sb can be derived from perfect fcc Sb by reducing the distance between alternating pairs of close packed planes, thereby lowering the symmetry of the crystal and doubling the size of the primitive unit cell. Perfect fcc Sb is predicted with HSE06 not to have a band gap. The band gap emerges as alternating pairs of (111) planes are shifted off center to form the A7 crystal structure (Figure 3). The addition of interstitial Li to the Sb host should shift the Fermi level into the conduction band. Again, the density of states increases very rapidly when moving into the conduction band suggesting that electrons donated by inserted Li are likely to be delocalized and itinerant due to the strong dispersion of the conduction bands.

Thermodynamic properties

An electrode material that undergoes path hysteresis will pass through metastable states for at least some portion of the charge and discharge process. While Sb, Li_2Sb and Li_3Sb are line compounds their crystal structures suggest that they can tolerate some degree of off stoichiometry, either by introducing interstitial Li in Sb, or by creating Li vacancies in Li_2Sb and Li_3Sb. To determine the accessibility of these metastable off-stoichiometric compositions, we calculated the free energies of dilute A7 Li_xSb, hexagonal $Li_{2-y}Sb$ and cubic $Li_{3-z}Sb$ using a cluster expansion approach.

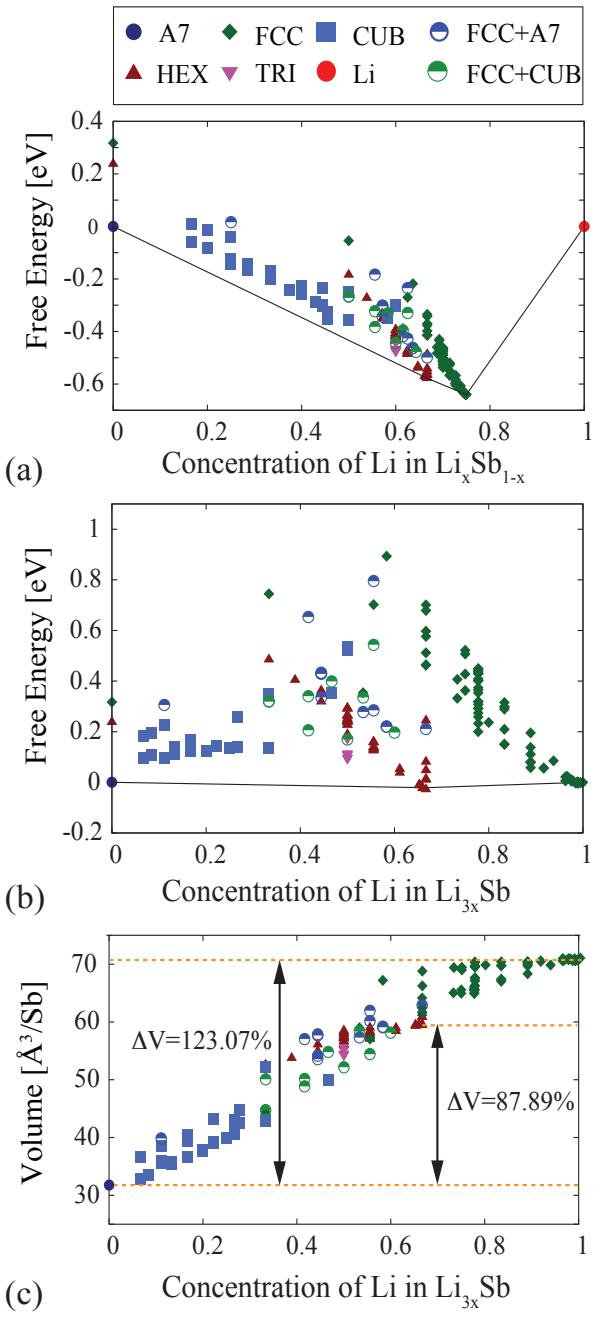

Figure 4: Formation energies of different configurations calculated from first-principles (a) per atom using pure Sb(A7) and Li as a reference. (b) per Sb using Li_3Sb and Sb(A7) as reference. The energies of the ground states are connected with a black line forming a convex hull. (c) Volume per Sb for all calculated structures between Sb and Li_3Sb. The changes in the volume of the ground state phases is shown with a dotted orange line.

As a first step in parameterizing cluster expansion Hamiltonians for each compound, we enumerated symmetrically distinct Li-vacancy orderings over the interstitial sites of A7 Sb and over the Li sites of hexagonal $Li_{2-y}Sb$ and cubic $Li_{3-z}Sb$. The Li-vacancy orderings were enumerated within symmetrically distinct supercells of the primitive unit cells of the parent compounds. We calculated the total energies of these configurations with DFT-PBE as implemented in VASP. Figure 4a shows the resulting formation energies, defined as

$$\Delta E(x) = E(x) - xE_{Li} - (1-x)E_{Sb} \qquad (2)$$

where, $E(x)$ is the DFT energy of a particular configuration in a supercell having concentration x. The energy $E(x)$ is normalized by the number of atoms within that supercell. E_{Li} and E_{Sb} are DFT energies per atom of bcc Li and A7 Sb respectively. The concentration x is a mole fraction, defined as the number of Li divided by the total number of atoms in the structure.

Figure 4b shows formation energies calculated relative to Sb and Li_3Sb and plotted versus Li concentration x as defined in $Li_{3x}Sb$. The energies of each structure in this plot is normalized by the number of Sb atoms. This figure more clearly illustrates the stability of the different metastable structures relative to the three ground states Sb, Li_2Sb and Li_3Sb. The volumes of the different structures are also shown in Figure 4c as a function of x in $Li_{3x}Sb$.

Figure 4a shows that hexagonal Li_2Sb, and cubic Li_3Sb are predicted to be stable intermediate compounds in the Li-Sb binary. Interestingly, configurations having very dilute vacancy concentrations over the octahedral sites of $Li_{3-z}Sb$ are also predicted to reside on the convex hull (e.g. $Li_{2.96}$ and $Li_{2.98}Sb$) Moreover, a large number of configurations with dilute concentrations of lithium vacancies in hexagonal Li_2Sb and cubic Li_3Sb have formation energies close to the convex hull.

The introduction of large vacancy concentrations in hexagonal Li_2Sb and cubic Li_3Sb often causes the original structure to relax to very different final structures. We have been able to distinguish between several categories of crystal structures that emerge when relaxing hexagonal Li_2Sb and cubic Li_3Sb upon removal of Li. The energies of these

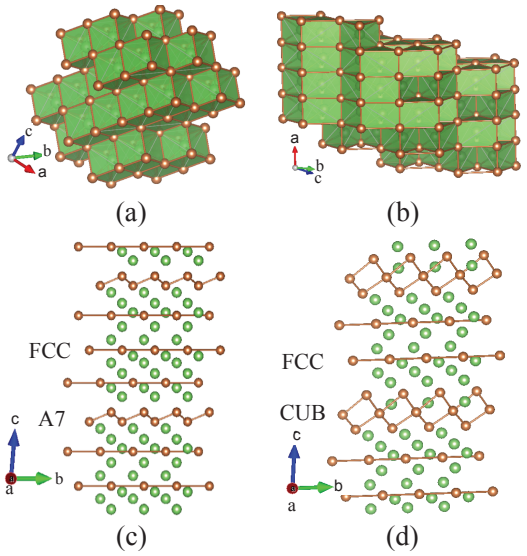

Figure 5: Examples of relaxed meta-stable structures upon creation of large vacancy concentrations in hexagonal Li_2Sb and cubic Li_3Sb or upon insertion of small lithium concentrations in A7 Sb. (a) CUB (LiSb) (b) TRI ($Li_{1.5}Sb$) (c) FCC+A7 (Li_2Sb) and (d) FCC+CUB ($Li_{1.8}Sb$)

structures are denoted by different symbols in Figure 4. The green diamonds (FCC) correspond to energies of structures in which the Sb sublattice of $Li_{3x}Sb$ maintains its fcc sublattice as in stoichiometric cubic Li_3Sb. The dark red triangles (HEX) correspond to structures in which the Sb sublattice is that of stoichiometric Li_2Sb. Addition of Li to Sb starting in the A7 crystal structure, even at very dilute Li concentrations, causes the Sb sublattice to adopt a cubic network as illustrated in Figure 5a. The energies of these structures are denoted with blue squares (CUB) in Figure 4. The pink triangles (TRI) having stoichiometry $Li_{1.5}Sb$ in Figure 4 consist of close-packed triangular Sb sublattices having an $A_tA_tA_t$ stacking sequence (as illustrated in Figure 5b). The Li occupy a subset of the trigonal prismatic interstitial sites within the Sb sublattice. For Li compositions between LiSb and Li_2Sb, a variety of hybrid structures emerge as shown in Figure 5c and 5d. The half-blue circles (FCC+A7) in Figure 4 correspond to the energies of layered structures that have several close packed triangular Sb layers as in fcc interleaved by a puckered Sb layer as in the A7 crystal structure of pure Sb (Figure 5c). The half-green circles (FCC+CUB) correspond to energies of structures

that are also layered, but have Sb triangular lattices interleaved by a layer made up of cubes of Sb as in the cubic structures of dilute Li_xSb (Figure 5d).

The formation energies of configurations having low vacancy concentrations within hexagonal Li_2Sb and cubic Li_3Sb were used to parameterize the expansion coefficients of cluster expansion Hamiltonians. Separate cluster expansions were constructed for hexagonal $Li_{2-y}Sb$ and cubic $Li_{3-z}Sb$ (where y and z is the number of Li vacancies per formula unit). In parameterizing a cluster expansion for cubic $Li_{3-z}Sb$, only configurations that maintained the fcc Sb sublattice after relaxation (FCC in Figure 4) were used, while in the parameterization of the cluster expansion for the hexagonal phase only configurations that maintained the Sb sublattice of Li_2Sb (HEX in Figure 4) were used. The cluster expansions were

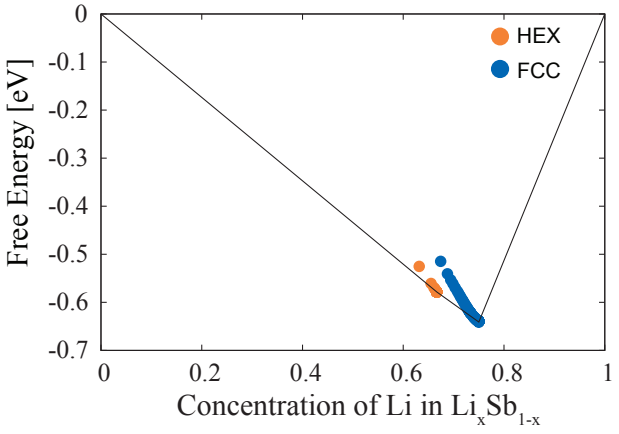

Figure 6: The calculated free energies of $Li_{2-y}Sb$ (HEX) and $Li_{3-z}Sb$ (FCC) at 300 K plotted as a function of mole fraction x in Li_xSb_{1-x}.

subjected to grand canonical Monte Carlo simulations to predict the dependence of the Li chemical potential on Li concentration within each compound. This dependence was then integrated to calculate the free energy as a function of Li concentration. The calculated free energies are shown in Figure 6.

The voltage of an electrochemical cell using metallic Li as the anode is related to the Li chemical potentials according to

$$\Phi(x) = -(\mu_{Li}(x) - \mu^o_{Li})/e \qquad (3)$$

where, $\mu_{Li}(x)$ is the Li chemical potential in Li_xSb_{1-x} and μ^o_{Li} is the Li chemical potential of metallic Li. The chemical potentials in Eq. 3 are in units of eV and e corresponds to the charge of an electron. Figure 7 shows the calculated equi-

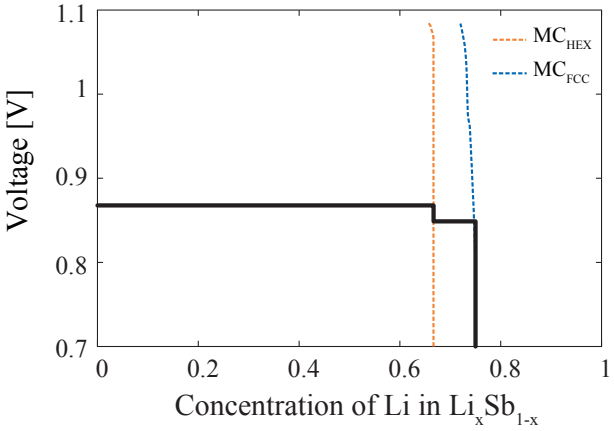

Figure 7: Metastable voltage profiles for $Li_{2-y}Sb$ (MC_{HEX}) and $Li_{3-z}Sb$ (MC_{FCC}). The calculated equilibrium voltage curve as a function of Li concentration is shown in black.

librium voltage curve as a function of Li concentration. A small step at the composition of Li_2Sb (x=0.66) separates two plateaus corresponding to two-phase reactions between Sb and Li_2Sb and between Li_2Sb and Li_3Sb respectively. The step height is approximately 50 mV. Figure 7 also shows metastable voltage profiles for $Li_{2-y}Sb$ and $Li_{3-z}Sb$. Cubic $Li_{3-z}Sb$ can reach high vacancy concentrations (z$\sim$0.5) with a 0.2V overpotential relative to the equilibrium Li_3Sb to Li_2Sb voltage plateau.

Kinetic properties

Li diffusion within the three stable compounds is an important property as it determines the rates with which the electrode can be charged and discharged and is likely to play a role in the selection of kinetic pathways. A key quantity in assessing the mobility of Li ions is the migration barrier of individual hops. Diffusion in most electrode materials for Li-ion batteries occurs at non-dilute concentrations and can be quite complex due to the dependence of migration barriers and hop mechanisms on the local concentration and the varying degrees of disorder among lithium and vacancies.[27,38] A treatment of non-dilute diffusion requires kinetic Monte Carlo approaches combined

with cluster expansion techniques, for example, to describe the dependence of atomic hop barriers on the local degree of Li-vacancy ordering.[27,39,40] Since A7 Sb, hexagonal Li_2Sb and Li_3Sb are essentially line compounds, however, we need only consider diffusion in the presence of very dilute concentrations of diffusion mediating defects such as Li interstitials or Li vacancies. The diffusion coefficient in these dilute limits is directly proportional to individual atomic hop frequencies,[38] which can be approximated with transition state theory.[41]

In A7 Sb, the relevant diffusion process is the migration of an isolated interstitial Li from one site to an adjacent interstitial site, while in hexagonal Li_2Sb and cubic Li_3Sb atomic diffusion is mediated through the migration of isolated vacancies and possibly divacancies between adjacent sites of the Li sublattices of the compounds. Using the nudged elastic band method as implemented in VASP, we calculated the migration barriers for elementary hops in A7 Sb, hexagonal Li_2Sb and Li_3Sb.

For nudged elastic band calculations of isolated interstitial Li hops in A7 Sb, we used a $3\times3\times2$ supercell of the hexagonal unit cell of A7 Sb, while for Li hops into isolated vacancies in Li_2Sb we used a $2\times2\times2$ supercell of the hexagonal unit cell. Nudged elastic band calculations for Li hops into isolated vacancies and divacancies in cubic Li_3Sb were performed with a $3\times3\times3$ supercell of the primitive cell of Li_3Sb.

At dilute Li concentrations, individual Li ions can occupy two distinct interstitial sites in A7 Sb: an eightfold coordinated site (3b), and a compressed octahedral site (3a). The eightfold 3b site is more stable than the compressed octahedral 3a site by $\sim$200 meV. Li can hop between adjacent sites, either by performing a curved hop by passing through an intermediate tetrahedral site or by following a direct hop as illustrated in Figure 8b and Figure 8d. The calculated migration barriers shown in Figure 8a and 8c, are high when compared to typical Li migration barriers in electrode materials for Li-ion batteries.[42] The connectivity of these hops forms a three-dimensional network, such that Li diffusion will be three dimensional.

There are two symmetrically distinct Li sites in hexagonal Li_2Sb, a tetrahedral site (6g) and a square pyramidal site (6h). An isolated vacancy prefers to reside in the 6g tetrahedral site. The energy increases by $\sim$40 meV when the vacancy moves from the tetrahedral site to the 6h square pyramidal site. Figure 9a shows the energy as a Li ion migrates from the square pyramidal site to a neighboring vacant tetrahedral site. Li can also hop between neighboring tetrahedral sites parallel the **c** axis and the energy for this hop is shown in Figure 9c. The migration barriers for both hops are of the order of 200-250 meV. Hops between neighboring tetrahedral sites or neighboring square pyramidal sites parallel to the basal plane of the hexagonal unit cell are also possible, however, the barriers for these hops are of the order of 1 eV and are therefore unlikely to contribute much to macroscopic Li diffusion. The collection of the symmetrically equivalent nearest neighbor hops with low barriers forms a three dimensional network.

The Li ions of Li_3Sb fill both the tetrahedral and octahedral interstitial sites of the fcc Sb sublattice. An isolated vacancy prefers to reside on the octahedral site. The energy of the crystal increases by 100 meV when the vacancy moves from the octahedral site to the tetrahedral site. The energy along the migration path as a Li atom hops from a tetrahedral site to an octahedral site is shown in Figure 10a. The energy barrier is less than 150 meV, a very small value. A similar migration barrier was recently predicted by Baggetto et al[21] for Li_3Sb. The calculated free energy for cubic $Li_{3-z}Sb$ shown in Figure 6 suggests that Li_3Sb can tolerate off stoichiometry and that vacancy clusters may be prominent. We therefore also considered Li hops into a divacancy. Figure 10c shows the energy as a Li hops from a tetrahedral site into a vacant octahedral site next to a vacant tetrahedral site. While vacancies in Li_3Sb prefer to reside on octahedral sites, when an octahedral vacancy is next to a tetrahedral vacancy the energy of the crystal actually decreases when a tetrahedral Li hops into the octahedral site, thereby forming two tetrahedral vacancies. The barrier for this hop, as for the single vacancy hop, is again very low and of the order of 150 meV.

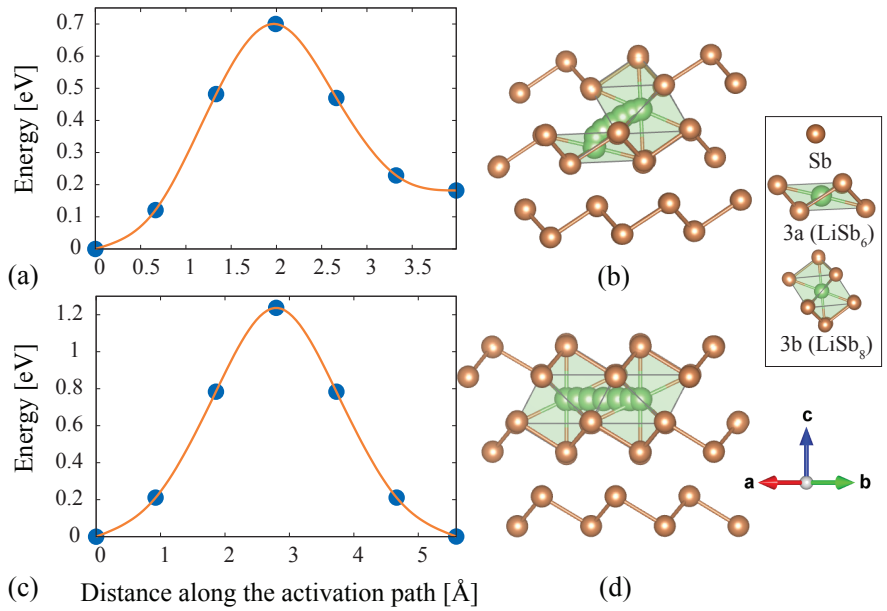

Figure 8: Migration barriers and paths for Li hops in A7 Sb at dilute Li concentrations. (a) and (b) Li hops from an eightfold coordinated site to adjacent a compressed octahedral site. (b) and (c) Li hops from an eightfold coordinated site to adjacent eightfold coordinated site directly.

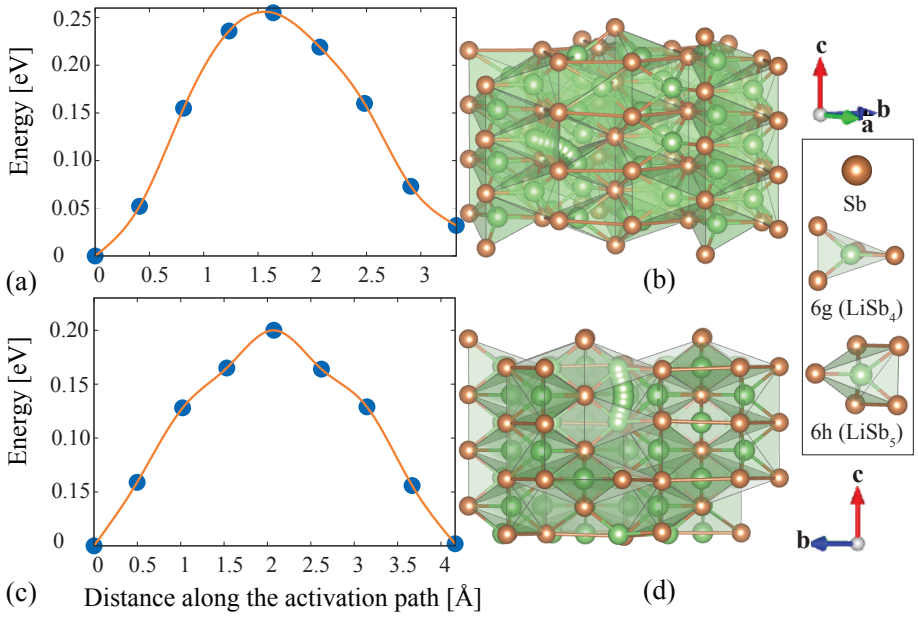

Figure 9: Migration barriers and paths for Li hops in hexagonal Li_2Sb. (a) and (b) Li hops from a square pyramidal site to adjacent vacant tetrahedral site. (b) and (c) Li hops between neighboring tetrahedral sites parallel to the **c** axis.

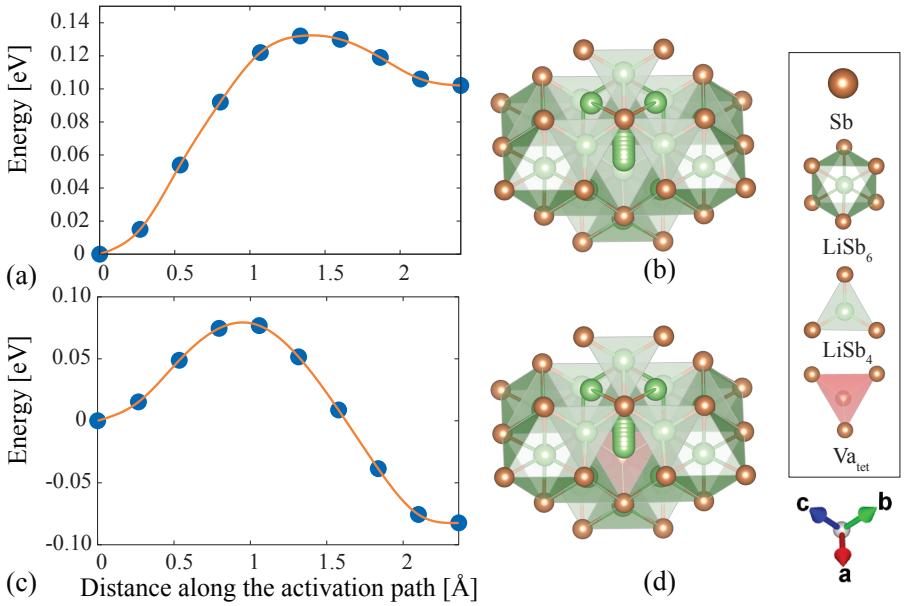

Figure 10: Migration barriers and paths for Li hops in fcc based Li_3Sb. (a) and (b) Li hops from a tetrahedral site to adjacent vacant octahedral site. (c) and (d) Li hops from a tetrahedral site into a vacant octahedral site next to a vacant tetrahedral site (Li hops into a divacancy).

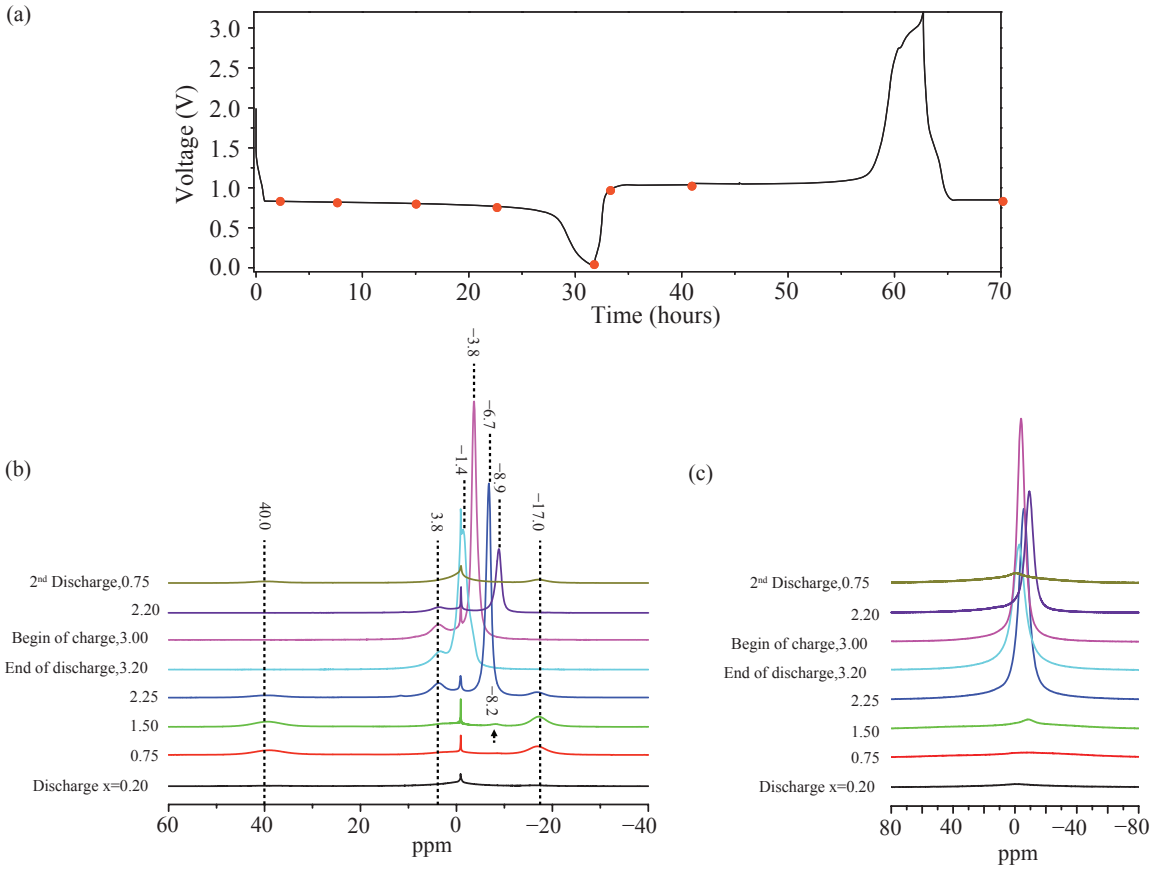

Figure 11: (a) Electrochemical curve of Li-Sb obtained at a cycle rate of C/30. A series of samples were stopped after discharging/charging to different states and extracted, as indicated by the red dots. The corresponding ^{7}Li static and MAS NMR spectra are shown in (b) and (c), respectively. All spectra were acquired at 9.4 T and a MAS rate of 30 kHz.

3.3 Electrochemical and NMR Measurements

Ex situ ^{7}Li NMR Studies A typical discharge/charge curve obtained for Sb/Li, using a cycle rate of C/30 (full capacity, in this case, equating to 3 Li per Sb in 30 hours), is shown in Figure 11(a). A series of samples were extracted from batteries stopped after discharging/charging to different states, as indicated by the red dots on the voltage-capacity profile. Samples are denoted as Li_xSb, where x denotes the Li content calculated from the discharging/charging time. The ^{7}Li MAS and static NMR spectra obtained for each sample are shown in Figures 11(b) and (c), respectively. In each MAS spectrum, a sharp and a broad resonance are observed at -1 ppm and 0 ppm. These are assigned to the electrolyte and solid electrolyte interphase (SEI), respectively.

Two resonances appear in a 1:1 ratio at 40 and -17 ppm in the MAS spectrum for the sample obtained at the beginning of discharge, corresponding to composition $Li_{0.2}Sb$. The intensities of both resonances increase until a maximum is reached after 15 hours of discharge, corresponding to a composition of $Li_{1.5}Sb$. Their intensities then decrease ($Li_{2.5}Sb$) until they disappear at the end of the first discharge ($Li_{3.2}Sb$). It is noted that these two resonances are absent from the following charge process but reappear during the second discharge. This behavior is consistent with the observation of Li_2Sb via in situ XRD studies.[20] Hence, the resonances at 40 and -17 ppm are tentatively assigned to the Li sites in Li_2Sb. This structure contains two Li sites with multiplicities of 1:1 consistent with the observed intensity ratio of 1:1.

During the first discharge, after 7.5 hours ($Li_{0.75}Sb$), two weak resonances appear at 3.8 and -8.5 ppm. The intensity of the resonance at -8.5 ppm increases upon further lithiation, while shifting towards positive chemical shift values: -8.2 ppm at $Li_{1.5}Sb$, -6.7 ppm at $Li_{2.25}Sb$ and -1.4 ppm at the end of discharge, $Li_{3.2}Sb$. During delithiation, this resonance returns to a negative chemical shift value (-8.9 ppm, during charge to $Li_{2.2}Sb$) and reduces in intensity. The resonance at 3.8 ppm, and the series of shifting resonances identified, are tentatively assigned to Li_3Sb.

To confirm the assignment of the resonances, two-dimensional ^{7}Li exchange NMR experiments were attempted for samples obtained during the first discharge, specifically those with compositions $Li_{1.5}Sb$ and $Li_{2.25}Sb$. These samples were selected for investigation because they contain all of the ^{7}Li NMR resonances observed during cycling. Using this technique it is possible to observe spin diffusion and chemical exchange between Li species in the same phase, i.e., it is a method used to determine whether resonances belong to the same phase. The ^{7}Li MAS NMR spectrum, and corresponding deconvolution, for $Li_{1.5}Sb$ are shown in Figure S1(a). In addition to the resonances assigned above, a weak resonance at 21 ppm is resolved. Two-dimensional (2D) ^{7}Li exchange NMR experiments, completed as a function of mixing time for $Li_{1.5}Sb$, indicate an asymmetric cross-peak correlating the resonances at 21 and -17 ppm (Figure S1(b)), even at 0.1 ms indicating they belong to the same phase. Clear correlations between the 40 and -17 ppm resonances are seen following a mixing time of 200 m. Using this, in conjunction with the information above, the resonances at 40, 21 and -17 ppm are assigned to Li_2Sb. The resonance at 21 ppm is believed to be due to low concentrations of Li vacancies or interstitials generated during lithiation. The asymmetric crosspeaks are tentatively ascribed to the short spin-lattice relaxation time for the 21 ppm resonance.[43] The presence of a non-stoichiometric Li_2Sb phase is consistent with the calculated free energy of Li_2Sb, which is very shallow and remains close to the common tangent as the Li concentration is reduced (Figure 6).

Cross peaks were also observed for the resonances at 3.8 and -8.2 ppm in the 200 ms 2D experiment, consistent with their assignment to the same phase (Li_3Sb). [6,7]^{7}Li NMR spectra were also acquired for $Li_{2.25}Sb$ (see the Supporting Information for more details) the results suggesting that the "Li_3Sb" phase at this composition gives rise to resonances at 3.5 and -6 ppm, with a very weak peak being seen at 7 ppm. However, the observed change in relative intensities for the 3.8 ppm peak and the negative peaks is not consistent with the 2:1 multiplicities of the tetrahedral and octahedral sites filled by Li in stoichiometric Li_3Sb. We, therefore, ascribe the shifts to the changes in electronic structure (and mobility) induced by non-

stoichiometry in Li_3Sb.

Static ^{7}Li NMR spectra (Figure 11(c)) were acquired to assist in assigning the resonances observed during subsequent in situ NMR studies. The resonances observed at 40 and -17 ppm during the MAS study cannot be observed and are presumably buried under the broad baseline. However, the series of shifting resonances observed ex situ can be monitored with relative ease via static NMR experiments, as demonstrated in Figure 11(c). This suggests that any changes in chemical shift observed during in situ NMR studies will provide valuable insight into the phases formed.

In situ ^{7}Li NMR Studies *In situ* ^{7}Li NMR studies were completed for the first cycle of a Li-Sb cell at a rate of C/30 (Figure 12). During in situ NMR experiments the appearance of resonances corresponding to Li metal and the electrolyte can make it difficult to accurately deconvolute spectra and identify any changes occurring. As a result, "difference spectra" are plotted for the spectra acquired between the two red dots denoted on the voltage-time profile in Figure 12. Each spectrum was obtained by subtracting the pristine spectrum, i.e., a background spectrum of the cell acquired before electrochemical cycling.

No obvious changes are observed during the first 10-15 hours of reaction, corresponding to the formation of Li_2Sb. This is consistent with the static ex situ NMR studies, where resonances corresponding to Li_2Sb were buried under the baseline. Upon further lithiation, a resonance at approximately 4 ppm appears and gradually increases until the end of discharge. This is in contrast to our ex situ NMR study, where resonances with different chemical shifts were observed at different depths of lithiation. During the first 5 hours of charge, the resonance at 4 ppm shifts gradually towards negative chemical shift, reaching approximately -10 ppm. Upon further delithiation, the resonance remains at -10 ppm and the intensity decreases until the end of charge, where it disappears completely.

The resonance observed at 4 ppm during discharge is assigned to stoichiometric Li_3Sb. The resonance that shifts from 4 to -10 ppm during charge and from -1.4 to -8.9 ppm during the ex situ study is assigned to an under-lithiated Li_3Sb phase, $Li_{3-z}Sb$. The exact value of the shift is correlated with z, a measure for the depth of lithiation. This is in good agreement with the first-principles calculated formation energies and free energy of $Li_{3-z}Sb$, and the suggestion that holes are created upon lithium removal from cubic Li_3Sb (see Figure 2(c)). Moreover, this agrees with the suggestion that the structure of Li_3Sb can tolerate some degree of off stoichiometry by introducing Li vacancies.

4 Discussion

Although the charge and discharge of Sb electrodes appears facile and stable over many cycles, it nevertheless exhibits path hysteresis.[19,20] The discharge voltage profile (i.e. Li insertion) has two plateaus with a small step corresponding to the formation of Li_2Sb, while the charge voltage profile (Li extraction) has a single plateau between Li_3Sb and Sb. The voltage interval in which Li_2Sb is stable relative to Sb and Li_3Sb is very small (~ 0.03V as predicted from first principles) and may not appear as a sharp step in experimental discharge voltage profiles. Nevertheless, there is a consistent difference of $\sim$ 0.2-0.3 V between charge and discharge with in-situ XRD indicating the formation of Li_2Sb upon discharge, but its absence during charge.[20] This behavior is confirmed with the ex-situ NMR measurements performed in this work.

Here we argue that a likely cause of path hysteresis in Li-Sb electrodes is a large asymmetry in the driving force for the nucleation of the intermediate Li_2Sb phase. A driving force for nucleation of a new phase β within a preexisting phase α can only emerge if α is supersaturated with respect to its equilibrium solubility limit x^α determined by the common tangent to the free energies of α and β as shown schematically in Figure 13a. This requires an overpotential $\Delta\Phi$ relative to the equilibrium voltage of the two-phase coexistence. The overpotential $\Delta\Phi$ can be represented graphically in a free energy versus concentration plot as illustrated in Figure 13a (since the intercept of the tangent to the free energy with the x_{Li}=1 axis corresponds to the Li chemical potential and the voltage is related to the Li chemical potential according to Eq. 3). As shown in Figure 13a, the driving force for the nucleation of a new phase, β, in a supersaturated phase, α, is equal to the distance between

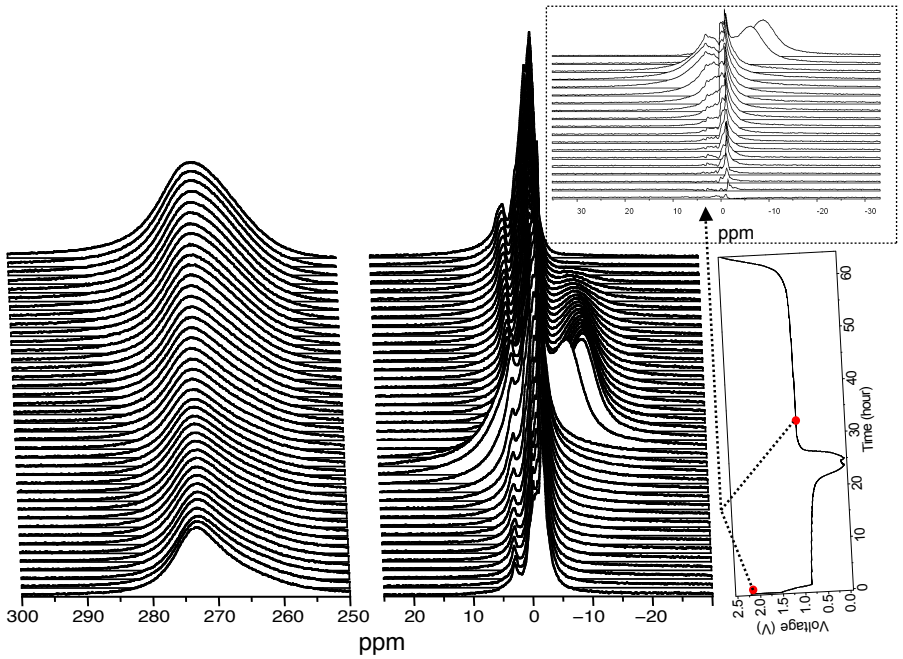

Figure 12: *In situ* ^{7}Li NMR spectra acquired for the Li-Sb system cycled at a rate of C/30. Signal corresponding to Li metal is shown at 273 ppm. "Difference spectra" are displayed in the inset for the region between the two red dots on the voltage-time curve. "Difference spectra" were obtained by subtracting the background spectrum of the cell before electrochemical cycling.

the free energy of β and the tangent to the free energy of the supersaturated α phase.[44]

Figure 13b graphically shows the nucleation driving forces for Li_2Sb and Li_3Sb in a supersaturated Sb phase when an overpotential of 0.1V relative to the equilibrium voltage plateau for the Sb to Li_2Sb reaction is imposed. As is clear from Figure 13b, the driving forces to nucleate Li_2Sb and Li_3Sb from a supersaturated Sb phase upon Li insertion are very similar. Figure 13c shows the nucleation driving forces for Li_2Sb and Sb when the an overpotential of 0.1V to extract Li from Li_3Sb is imposed relative to the equilibrium voltage of the Li_3Sb to Li_2Sb reaction. In this case, the driving force to nucleate Sb is substantially larger than that to nucleate Li_2Sb. The much larger difference in concentration between Sb and Li_3Sb compared to that between Li_2Sb and Li_3Sb results in a lever effect that significantly enhances the nucleation driving force for Sb relative to that for Li_2Sb.

The lever effect becomes more apparent when the driving force for nucleation is plotted as a function of over potential. Figure 13d shows the nulceation driving force for Li_2Sb and Li_3Sb when an overpotential to insert Li is applied to Sb. Since the concentrations of Li_2Sb and Li_3Sb are very close to each other, the nucleation driving forces for both phases are almost identical in value, especially for large over potentials. The situation is very different when applying an overpotential to extract Li from Li_3Sb, as shown in Figure 13e. The driving force for the nucleation of Sb exceeds that of Li_2Sb already at overpotentials as small as 0.03 eV. The insertion of Li into Sb, therefore, results in comparable driving forces for Li_2Sb and Li_3Sb at all but the smallest overpotentials while the extraction of Li from Li_3Sb very quickly produces much larger driving forces for the nucleation of Sb than for Li_2Sb.

The thermodynamic and kinetic properties calculated in this work along with the NMR observations also suggest that much higher overpotentials are readily accessible in Li_3Sb than in Sb. The predicted Li mobility at dilute concentrations within the A7 crystal structure of Sb is very low, with migration barriers around 0.7 eV and above. Hence, Sb will be slow to reach high levels of supersaturation with respect to the Li concentration. The predicted Li mobility in Li_3Sb in contrast is very high, with migration barriers ranging

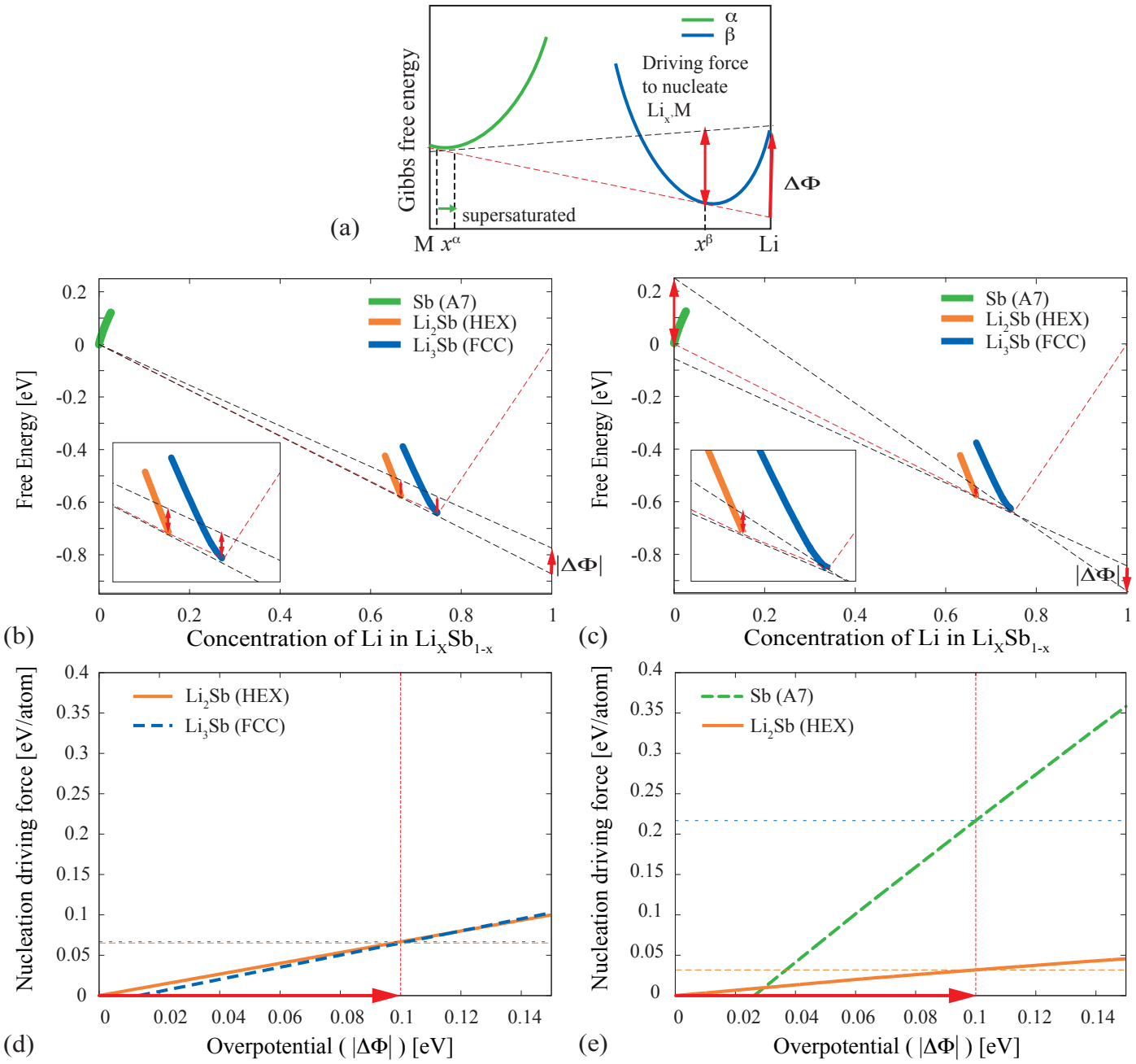

Figure 13: (a) Schematic illustration of the driving force for the nucleation of a new phase (β) in a supersaturated phase (α). (b) The nucleation driving forces for Li_2Sb and Li_3Sb in Sb(A7) phase during discharge reaction. (c) The nucleation driving forces for Li_2Sb and Sb in Li_3Sb phase during charge reaction. (d)-(e) The nucleation driving forces as a function of overpotential in discharge and charge reactions respectively.

between 0.1 to 0.13 eV. These migration barriers are lower even than those encountered in intercalation compounds.[42] Li can therefore be extracted very rapidly from Li_3Sb and in large numbers, resulting in high overpotentials. This is supported by the in-situ NMR measurements, which show that Li extraction from Li_3Sb results in large off-stoichiometry. As shown in Figure 13e, the easily accessible high overpotentials in Li_3Sb in turn translate into much larger driving forces for Sb nucleation than for Li_2Sb nucleation with the consequence that Li_3Sb transforms directly to Sb, bypassing the intermediate Li_2Sb phase.

As with path hysteresis in $CuTi_2S_4$, a model displacement reaction analyzed using a first-principles multi-scale approach,[16] path hysteresis in the Li-Sb alloying reaction arises from a very high Li diffusion coefficient in the fully lithiated phase. The kinetic ease of extracting Li from the fully lithiated phase renders a metastable path kinetically more accessible than the true equilibrium path. The lever effect on the nucleation driving forces then likely leads to the nucleation of Sb rather than the thermodynamically more stable intermediate Li_2Sb phase. In the Li-Sb system, path hysterisis upon charge (i.e. Li extraction) should be avoidable if Li extraction occurs sufficiently slowly in a voltage window where a driving force to nucleate Li_2Sb exists but where a similar driving force to nucleate Sb is not present. Since Li_2Sb is thermodynamically stable in only a very small voltage window, path hysteresis may be difficult to suppress using realistic charge rates.

The phase transformation mechanisms in the Li-Sb system remain unclear. While the calculated properties allow us to speculate, a true understanding of the precise phase transformation mechanisms will likely only emerge with the help of in-situ TEM experimental observations. Our study indicates that the electrochemical reaction of Li with Sb, although classified as an alloying reaction, also has much in common with intercalation processes. As described in Section 3.1, Sb, Li_2Sb and Li_3Sb are crystallographically similar. Furthermore, the crystal structures of the lithiated compounds easily facilitate interstitial diffusion as opposed to substitutional diffusion common to most alloys.[45] In fact the Li mobility in Li_2Sb and Li_3Sb are predicted to be very high with migration barriers as low as 0.1 eV.

The commonality in crystal structures between Sb, Li_2Sb and Li_3Sb, suggests the possibility that two phase reactions between these phases could occur coherently, or at least semi-coherently. In general, coherent two-phase coexistence is more desirable than a reconstructive two-phase reaction where a disordered interface separates the new phase from the original phase. Reconstructive two-phase reactions are more likely to cause drastic morphological changes of the original electrode particles during cycling as occurs with Si electrodes. A comparison of the eigenvalues of the transformation strains linking pairs from among Sb, Li_2Sb and Li_3Sb suggest that only a two-phase coexistence between Li_2Sb and Li_3Sb may possibly be energetically viable. While the eigenvalues of the transformation strains do not satisfy the strict criteria for a strain invariant plane common to both Li_2Sb and Li_3Sb, they do come close, with one eigenvalue being positive, another eigenvalue being negative and a third eigenvalue being close to zero, differing from zero by 1.3%.

5 Conclusion

The aim of this work was to identify the origin of phase transformation hysteresis during the electrochemical cycling of Sb electrodes in Li-ion batteries. The phases that form during the electrochemical reaction of Li with Sb electrodes (Sb, Li_2Sb and Li_3Sb) are crystallographically very similar, yet their transformation strains are large making it unlikely that two-phase reactions between any pair of phases occurs coherently. Hybrid functional HSE06 calculations predict that Sb and Li_3Sb are semiconductors while Li_2Sb is a metal. While Li_2Sb and Li_3Sb are line compounds in the Li-Sb phase diagram, our first-principles statistical mechanical analysis suggests that they can tolerate high concentrations of Li vacancies without incurring a large free energy penalty. Calculations of Li migration barriers predict that Li has a very low mobility in A7 Sb, having to overcome migration barriers of the order of 0.7 eV. Li is, however, predicted to be remarkably mobile in Li_3Sb and Li_2Sb with migration barriers between 0.15 and 0.25 eV. An analysis of nucleation driving forces

reveals a large lever effect upon Li removal from Li_3Sb, with the nucleation driving force for Sb exceeding that for Li_2Sb already at small overpotentials. This, together with a very high Li mobility in Li_3Sb, which facilitates large overpotentials, provides an explanation for the phase transformation hysteresis observed when cycling Sb electrodes.

Acknowledgement This work was supported by the Northeastern Center for Chemical Energy Storage, an Energy Frontier Research Center funded by the U.S Department of Energy, and the Office of Basic Energy Science under award No. DE-SC0001294. The first-principles calculations were performed using computational resources provided by the National Energy Research Scientific Computing Center (NERSC), supported by the Office of Science and U.S. Department of Energy, under Contract Number DE-AC02-05CH11231. Images of crystal structures were produced with VESTA.[46]

References

(1) Whittingham, M. S. *Chemical Reviews* **2004**, *104*, 4271–4302.

(2) Tarascon, J.; Armand, M. *Nature* **2001**, *414*, 359–367.

(3) Poizot, P.; Laruelle, S.; Grugeon, S.; Dupont, L.; Tarascon, J. *Nature* **2000**, *407*, 496–499.

(4) Thackeray, M.; Vaughey, J.; Johnson, C.; Kropf, A.; Benedek, R.; Fransson, L.; Edstrom, K. *J. Power Sources* **2003**, *113*, 124–130.

(5) Morcrette, M.; Rozier, P.; Dupont, L.; Mugnier, E.; Sannier, L.; Galy, J.; Tarascon, J. *Nat. Mater.* **2003**, *2*, 755–761.

(6) Bruce, P. G.; Freunberger, S. A.; Hardwick, L. J.; Tarascon, J.-M. *Nat. Mater.* **2012**, *11*, 19–29.

(7) Lu, Y.-C.; Gallant, B. M.; Kwabi, D. G.; Harding, J. R.; Mitchell, R. R.; Whittingham, M. S.; Shao-Horn, Y. *Energy Environ. Sci.* **2013**, *6*, 750–768.

(8) Girishkumar, G.; McCloskey, B.; Luntz, A. C.; Swanson, S.; Wilcke, W., *J. Phys.Chem. Lett.* **2010**, *1*, 2193–2203.

(9) Evers, S.; Nazar, L. F. *Acc. Chem. Res.* **2013**, *46*, 1135–1143.

(10) Hatchard, T.; Dahn, J. *J. Electrochem. Soc.* **2004**, *151*, A838–A842.

(11) Winter, M.; Besenhard, J. O. *Electrochim. Acta.* **1999**, *45*, 31 – 50.

(12) Huggins, R. A. *J. Power Sources* **1999**, *81*, 13 – 19.

(13) Bruce, P. G.; Scrosati, B.; Tarascon, J.-M. *Angewandte Chemie International Edition* **2008**, *47*, 2930–2946.

(14) Park, C.-M.; Kim, J.-H.; Kim, H.; Sohn, H.-J. *Chem. Soc. Rev.* **2010**, *39*, 3115–3141.

(15) Doe, R. E.; Persson, K. A.; Meng, Y. S.; Ceder, G. *Chem. Mater.* **2008**, *20*, 5274–5283.

(16) Yu, H.-C.; Ling, C.; Bhattacharya, J.; Thomas, J. C.; Thornton, K.; Van der Ven, A. *Energy Environ. Sci.* **2014**, *7*, 1760–1768.

(17) Van der Ven, A.; Garikipati, K.; Kim, S.; Wagemaker, M. *J. Electrochem. Soc.* **2009**, *156*, A949–A957.

(18) Mukhopadhyay, A.; Sheldon, B. W. *Prog. Mater. Sci.* **2014**, *63*, 58–116.

(19) Park, C.-M.; Yoon, S.; Lee, S.-I.; Kim, J.-H.; Jung, J.-H.; Sohn, H.-J. *J. Electrochem. Soc.* **2007**, *154*, A917–A920.

(20) Hewitt, K.; Beaulieu, L.; Dahn, J. *J. Electrochem. Soc.* **2001**, *148*, A402–A410.

(21) Baggetto, L.; Ganesh, P.; Sun, C.-N.; Meisner, R. A.; Zawodzinski, T. A.; Veith, G. M. *J. Mater. Chem. A* **2013**, *1*, 7985–7994.

(22) Perdew, J. P.; Burke, K.; Ernzerhof, M. *Phys. Rev. Lett.* **1996**, *77*, 3865–3868.

(23) Kresse, G.; Furthmüller, J. *Phys. Rev. B* **1996**, *54*, 11169–11186.

(24) Kresse, G.; FurthmÃijller, J. *Comput. Mater. Sci.* **1996**, *6*, 15 – 50.

(25) Kresse, G.; Joubert, D. *Phys. Rev. B* **1999**, *59*, 1758–1775.

(26) Blöchl, P. E. *Phys. Rev. B* **1994**, *50*, 17953–17979.

(27) Van der Ven, A.; Thomas, J. C.; Xu, Q.; Swoboda, B.; Morgan, D. *Phys. Rev. B* **2008**, *78*.

(28) Van der Ven, A.; Thomas, J. C.; Xu, Q.; Bhattacharya, J. *Math. Comput. Simul.* **2010**, *80*, 1393–1410.

(29) Henkelman, G.; Jonsson, H. *J. Chem. Phys.* **2000**, *113*, 9978–9985.

(30) Krukau, A. V.; Vydrov, O. A.; Izmaylov, A. F.; Scuseria, G. E. *J. Chem. Phys.* **2006**, *125*, 224160.

(31) Key, B.; Bhattacharyya, R.; Morcrette, M.; Seznec, V.; Tarascon, J.-M.; Grey, C. P. *J. Am. Chem. Soc.* **2009**, *131*, 9239–9249.

(32) Sangster, J.; Pelton, A. *J. Phase Equilib.* **1993**, *14*, 514–517.

(33) Muller, W. *Z. Naturforsch. B.* **1977**, *32*, 357–359.

(34) Brauer, G.; Zintl, F. *Z. Phys. Chem. B-Chem. E.* **1937**, *37*, 323–352.

(35) Hickman, B. S. *J. Mater. Sci* **1969**, *4*, 554–563.

(36) Usikov, M.; Zilbershtein.VA, *Phys. Status Solidi A* **1973**, *19*, 53–58.

(37) KhachaturiÍąan, A. G. *Theory of structural transformations in solids*; Wiley: New York, 1983.

(38) Van der Ven, A.; Bhattacharya, J.; Belak, A. A. *Acc. Chem. Res.* **2013**, *46*, 1216–1225.

(39) Van der Ven, A.; Ceder, G.; Asta, M.; Tepesch, P. D. *Phys. Rev. B* **2001**, *64*, 184307.

(40) Bhattacharya, J.; Van der Ven, A. *Phys. Rev. B* **2011**, *83*.

(41) Vineyard, G. H. *J. Phys. Chem. Solids* **1957**, *3*, 121–127.

(42) Van der Ven, A.; Ceder, G. *Electrochem. Solid-State Lett.* **2000**, *3*, 301–304.

(43) Chaudhuri, S.; Wang, F.; Grey, C. *JOURNAL OF THE AMERICAN CHEMICAL SOCIETY* **2002**, *124*, 11746–11757.

(44) Balluffi, R. W.; Allen, S. M.; Carter, W. C. *Kinetics of Materials*; John Wiley Sons, Inc., 2005; pp 459–499.

(45) Van der Ven, A.; Yu, H.-C.; Ceder, G.; Thornton, K. *Prog. Mater. Sci.* **2010**, *55*, 61–105.

(46) Momma, K.; Izumi, F. *J.Appl.Crystallogr.* **2008**, *41*, 653–658.